Laser Beam Smoothing Caused by the Small-Spatial-Scale *B*-Integral

Introduction

Target irradiation uniformity is an important aspect of the direct-drive approach to inertial confinement fusion (ICF),[1,2] where the capsule is directly irradiated by a symmetrically arranged cluster of high-intensity, ultraviolet (UV) laser beams. Nonuniformity in laser irradiation seeds the Rayleigh–Taylor hydrodynamic instability, which consequently degrades target performance.[3,4] Various techniques are employed on the OMEGA[5] laser to improve the on-target irradiation uniformity to reduce laser imprint: two-dimensional smoothing by spectral dispersion (2-D SSD),[6–8] distributed phase plates (DPP's),[9,10] polarization smoothing (DPR's),[5,11,12] and multiple-beam overlap. A complete understanding of the laser focal-spot dynamics is essential to ICF performance, and it provides valuable feedback as a laser diagnostic tool. In Ref. 13, the smoothing rate of 2-D SSD on OMEGA was investigated both experimentally and numerically. Excellent agreement between the experimental results and the corresponding simulations was found for all 2-D SSD cases and for low-energy shots without applied frequency modulation (FM) (i.e., without SSD). Laser beam smoothing of high-power glass lasers caused by small-spatial-scale and whole-beam *B*-integral effects with DPP's and no applied FM is examined in this article.

In the absence of externally applied FM, the beam can acquire bandwidth because of the time-dependent *B*-integral (Ref. 14, p. 385) acquired in the laser chain. The phase difference between a wave traveling in a vacuum and a wave propagating a distance *L* in a nonlinear medium in the *z* direction can be expressed as

$$\Delta\varphi = \frac{2\pi(n_0-1)L}{\lambda_0} + \phi_B(z),$$

where λ_0 is the vacuum wavelength, n_0 is the linear index of refraction, and *B* is the intensity dependent phase given by

$$\phi_B(z) = \frac{2\pi}{\lambda}\int_0^L \gamma\, I(z)\,dz,$$

where γ is the nonlinear constant of the medium and $I(z)$ is the intensity (compare Ref. 15). In the event that the *B*-integral is nonuniform in space and time, it will cause the speckle pattern produced by the DPP to move in the target plane, similar to the effect of SSD. In the absence of a smoothing mechanism such as SSD, the nonuniformity of the measured far fields with DPP's is expected to have an rms value of 100%, reflecting the high contrast of the speckle pattern produced by the presumed coherent illumination of the DPP. Experimental far-field measurements, however, acquired on OMEGA with the ultraviolet-equivalent-target-plane (UVETP) diagnostic of high-energy shots without applied FM yielded smoothed far fields with overall nonuniformity ranging from 62% to 88%.[13] The nonuniformity decreases approximately linearly with increasing average intensity. The amount of smoothing provided by *B*-integral effects alone is not sufficient for direct-drive ICF.[7] However, shots without applied FM are base-line measurements for the high-intensity SSD shots and are therefore studied in this article.

The dominant smoothing mechanism in pulses without externally applied FM is attributed to the small-spatial-scale *B*-integral variation, which possesses sufficient temporal bandwidth and beam divergence to affect OMEGA target spherical-harmonic modes as small as $\ell \sim 40$ or wavelengths as long as $\lambda_{\text{mode}} \sim 80\ \mu\text{m}$ (ℓ modes are related to wavelength by $\ell \equiv 2\pi r/\lambda_{\text{mode}}$, where $r = 0.5$ mm is the target radius). The small-spatial-scale *B*-integral results from intensity nonuniformities as the laser beam propagates through a nonlinear medium, such as amplifier glass, and produces amplitude and phase modulations in the beam (see Ref. 14, p. 381). This effect introduces time-dependent phase variations across the beam, which results in some smoothing of the speckle structure when the beam, without externally applied FM, passes through a DPP and is focused onto the target. The whole-beam *B*-integral affects smoothing to a smaller degree and is produced as the whole beam self-focuses (see Ref. 14, p. 380). The *RAINBOW* code (compare Ref. 15, p. 229) calculates the whole-beam *B*-integral for the pulse shapes used on OMEGA as a function of radius and time. It is shown later in the **Laser Beam**

Smoothing section that the whole-beam *B*-integral produces only a small portion of the observed smoothing because of its small temporal bandwidth coupled to the fact that its imposed laser divergence does not change substantially over time. As a result, the spatiotemporal evolution of the whole-beam *B*-integral is not sufficient to cause rapid movement of the speckle pattern in the far field. The whole-beam *B*-integral changes the on-target focal-spot diameter and shape by a small amount.

The transverse spatial-intensity profile of the near field evolves slowly in time from a center-peaked beam to an edge-peaked beam as a result of gain saturation effects. The highest far-field spatial frequencies produced by coherent illumination of the DPP are caused by the interference from the outer edges of the beam. Consequently, as the effective beam radius increases in time, the energy in the highest spatial frequencies increases. The effective radius of the fluence accurately yields the overall high-frequency cutoff.

The code *Waasikwa'*,[*] was developed to simulate the planar, time-integrated far fields produced by the OMEGA laser, which allows a direct comparison of the calculations to the images acquired by the UVETP diagnostic. *Waasikwa'* is a general-purpose simulation program that has the capability to model far fields under a variety of near-field conditions: arbitrary spatial envelopes that possess an arbitrary temporal envelope at any transverse point; whole-beam and small-spatial-scale *B*-integral near-field phase; 2-D SSD; arbitrary static phase aberrations; DPR's; the inherent bandpass characteristic of frequency conversion; and multiple-beam overlap. *Waasikwa'* utilizes the continuous DPP employed on OMEGA. In addition, it can be configured to run within a shared-memory model as a multiprocessing task on a parallel machine such as the SGI Origin 2000.[16]

The following sections describe far-field simulation and analysis, experimental results, simulation results, and conclusions.

Far-Field Simulation and Analysis

Waasikwa' calculates the far-field fluence using

$$F\left(x_{\text{ff}}, y_{\text{ff}}\right) \equiv \int_{\substack{\text{pulse} \\ \text{duration}}} I_{\text{ff}}\left(x_{\text{ff}}, y_{\text{ff}}, t\right) dt, \qquad (1)$$

---

[*]An Anishinaabe word meaning "polishes it" as in smoothing a rough surface. Resource: J. Nichols and E. Nyholm, eds. *Ojibwewi-ikidowinan and Ojibwe Word Resource Book*, Occasional Publications in Minnesota Anthropology, No. 7 (Minnesota Archaeological Society, St. Paul, MN, 1979).

where $I_{\text{ff}}\left(x_{\text{ff}}, y_{\text{ff}}, t\right)$ represents the instantaneous far-field intensity. The evolution of the far-field intensity is calculated by taking the modulus squared of a two-dimensional spatial Fourier transform of the UV near field (compare Goodman, Ref. 17, p. 83),

$$I_{\text{ff}}\left(x_{\text{ff}}, y_{\text{ff}}, t\right)$$

$$\equiv \left| \iint_{\forall\,\text{space}} E(x, y, t) e^{-i\frac{2\pi}{\lambda_{\text{UV}} f_{\Omega}}\left(x_{\text{ff}}x + y_{\text{ff}}y\right)} dx\, dy \right|^2, \qquad (2)$$

where $E(x,y,t)$ represents the complex-valued UV electric field strength in the near field and (x,y) and $(x_{\text{ff}}, y_{\text{ff}})$ are the near- and far-field coordinate systems, respectively; $\lambda_{\text{UV}} = 351$ nm is the UV vacuum wavelength; and $f_{\Omega} = 180$ cm is the focal length of the OMEGA focusing lens. The spatiotemporal evolution of the complex-valued UV electric field can be expressed as

$$E(x, y, t) \equiv E_0(x, y, t) e^{i\phi_B(x,y,t)} e^{i\phi_{\text{DPP}}(x,y)}, \qquad (3)$$

where $E_0(x,y,t)$ defines the electric field envelope of the pulsed beam; $\phi_B(x,y,t)$ represents the combined phase contributions of the whole-beam and small-spatial-scale intensity-dependent *B*-integral; and $\phi_{\text{DPP}}(x,y)$ is the static DPP phase-plate contribution whose mapping to the far field depends on its design. During OMEGA laser shots, the near fields of the 1- to 3-ns square pulses evolve from a center-peaked to an edge-peaked spatial-intensity profile. The near field of a 100-ps pulse, however, remains center peaked for the duration of the pulse. The spatiotemporal evolutions of both the Gaussian and square pulses are calculated with *RAINBOW* and are used as inputs to the *Waasikwa'* simulations. The equivalent near-field radius and pulse width are useful for calculating the average intensity and are defined as (see discussion of equivalent widths in Ref. 18, p. 148)

$$r_{\text{eq}} \equiv \frac{1}{F_{\text{nf}}(0)} \int_0^{\infty} F_{\text{nf}}(r)\, dr \qquad (4)$$

and

$$t_{\text{eq}} \equiv \frac{1}{P\left(t_c\right)} \int_{-\infty}^{\infty} P(t)\, dt, \qquad (5)$$

respectively, where the near-field fluence is defined by

$$F_{nf}(r) \equiv \int_{\forall t} |E_0(r,t)|^2 \, dt,$$

the near-field power is defined by

$$P(t) \equiv 2\pi \int_0^\infty r |E_0(r,t)|^2 \, dr,$$

and the pulse centroid is given by

$$t_c = \frac{\int_{-\infty}^{\infty} tP(t)\,dt}{\int_{-\infty}^{\infty} P(t)\,dt}.$$

It has been assumed that, for these calculations, the beam profile is azimuthally symmetric so that the spatial energy centroid is always located at $r = 0$. The equivalent widths permit a comparison of the shorter, 100-ps pulses (which have a center-peaked beam profile and a Gaussian pulse shape) to the longer pulses (which are, on the average, nearly square in space and time).

The 2-D power spectral density (2-D power spectrum or simply the 2-D psd) is derived from either the measured or simulated far-field fluences by taking the modulus squared of the 2-D spatial Fourier transform, namely,

$$\mathrm{PSD}\left(k_{x_{ff}}, k_{y_{ff}}\right)$$

$$\equiv \left| \iint_{\forall \, \text{far field}} F(x_{ff}, y_{ff}) e^{-i\left(k_{x_{ff}} x_{ff} + k_{y_{ff}} y_{ff}\right)} dx_{ff}\, dy_{ff} \right|^2, \quad (6)$$

where $F(x_{ff}, y_{ff})$ represents the far-field fluence as defined by Eq. (1), (x_{ff}, y_{ff}) is the far-field coordinate system, and $\left(k_{x_{ff}}, k_{y_{ff}}\right)$ is the far field's spatial-frequency coordinate system. The azimuthal sum at each radial wave number of the 2-D power spectrum defines the 1-D power spectral density (1-D power spectrum or simply the 1-D psd) and is given by

$$\mathrm{psd}(k_{ff}) \equiv \oint \mathrm{PSD}\left(k_{x_{ff}}, k_{y_{ff}}\right) k_{ff}\, d\theta, \quad (7)$$

where the transformation into polar coordinates is defined as $k_{ff} \equiv \sqrt{k_{x_{ff}}^2 + k_{y_{ff}}^2}$ and $\tan\theta \equiv k_{y_{ff}}/k_{x_{ff}}$. The single-beam irradiation nonuniformity σ_{rms} is defined as the square root of the ratio of the speckle power [e.g., the high frequencies $k_{ff} \geq 0.04$ (rad/μm) at the OMEGA target plane or ℓ modes with $\ell \geq 20$] to the envelope power of the far-field spot [i.e., the low frequencies $k_{ff} < 0.04$ (rad/μm)]. The envelope/speckle dividing-line wave number of 0.04 (rad/μm) represents the lowest spatial frequency that is smoothed by 2-D SSD, as discussed in Ref. 13. A finite entrance pupil imposes a limitation on the spatial-frequency bandwidth of an optical system (compare the intensity-impulse response or point-spread function of a diffraction-limited system with a circular exit-pupil function in Ref. 17, p. 110). On OMEGA, the highest spatial frequency of the laser speckle (or interference pattern) is limited by the finite diameter of the serrated apodizer, regardless of the beam profile. The OMEGA entrance pupil is defined by the diameter of the serrated aperture, which is located near the end of the laser driver section on OMEGA. The entrance pupil is imaged to the end of OMEGA and sets the final exit pupil to a full-system diameter $D_\Omega = 27.5$ cm. Consequently, the power spectrum possesses an absolute cutoff wave number that corresponds to the f-number limited spatial frequency

$$k_{cut_{ff}} = \frac{2\pi}{1.22} \frac{D_\Omega}{\lambda_{UV} f_\Omega} = 2.24 \left[\frac{\mathrm{rad}}{\mu\mathrm{m}}\right]$$

and corresponds to $\lambda_{mode_{cut}} = 280\,\mu$m.

Experimental constraints restrict the analysis to the central portion of the laser beam. Consequently, data windowing must be employed to accurately analyze the PSD of the data. Otherwise, when the 2-D PSD is calculated, the result contains Fourier artifacts of the cropping function convolved with the desired underlying power spectrum of the far field. A 2-D generalization of the common Hamming (the Hamming function does not go to zero like the similar Hanning function)[19] windowing function is employed:

$$\mathrm{SQHamming}\left(x_{ff}, y_{ff}\right)$$

$$\equiv \mathrm{Hamming}\left(x_{ff}\right) \cdot \mathrm{Hamming}\left(y_{ff}\right). \quad (8)$$

Experimental Results

A full description of the CCD-based UVETP diagnostic can be found in Ref. 13. An example of an acquired image of a 300-J, 3.5-ns shot with no applied FM is presented in

Fig. 82.34, where a lineout through the center of the beam is overplotted to show the highly modulated intensity. The laser-beam focus is centered nominally on the photodetector, and a 584-μm central portion of the whole 950-μm far-field spot (defined as the 95% enclosed energy contour) is captured on a 1024×1024-pixel grid. However, experimental variances of the far-field centroid require that the image be cropped to guarantee a consistent area for all shot data; a 720×720-pixel portion around the far-field centroid yields a 411×411-μm^2 area of the original image for analysis.

584 μm

TC5338
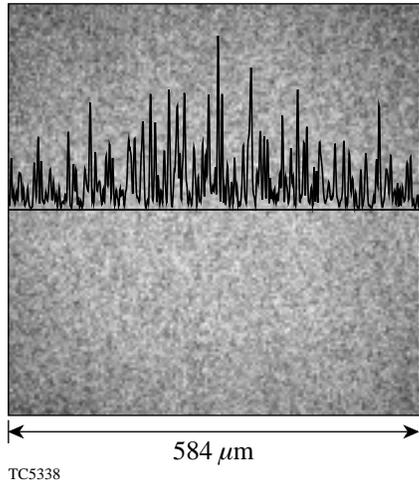
Figure 82.34
UVETP sampled far-field spot demonstrating the 46×, high-magnification setup. The image represents a 300-J, 3.5-ns square laser pulse without applied FM. As demonstrated with the single-pixel lineout through the center of the beam, the spot possesses a highly modulated intensity profile. The laser beam focus is centered nominally on the photodetector, and a 584-μm central portion of the whole 950-μm far-field spot (defined as the 95% enclosed energy contour) is captured on a 1024×1024-pixel grid.

Waasikwa' simulations use a different scale that samples the majority of the far-field spot to avoid aliasing effects from the Fourier transforms in Eq. (2). The far-field spot is calculated over a 1024×1024-pixel grid that spans a 993×993-μm^2 area. The speckle structure is resolved by surrounding the DPP data (defined as a 512×512-pixel grid covering 32.6×32.6-cm^2 area) with a zero buffer of 256 pixels on each side, forming a total near-field grid of 1024×1024 pixels. For a direct comparison of power spectra, the simulated far fields are cropped to match the area of the cropped UVETP images so that they span 424×424 pixels or a 411×411-μm^2 area. Consequently, the power spectrum frequency spacing for either the measurement or simulation is equivalent, i.e., $dk_{ff} = 0.0153$ (rad/μm), because the total sampled area of the

far field dictates the discrete Fourier domain spacing of the power spectrum.

The aforementioned configurations are used for all of the UVETP images and *Waasikwa'* simulations presented in this article. A 1-D power spectrum is calculated for each measured UVETP image and *Waasikwa'* simulation using the square Hamming window. The analysis results for all of the measured and simulated far fields discussed here are compiled in Table 82.IV.

The measured nonuniformity for the high- and low-energy shots without applied FM decreases approximately linearly with increasing average near-field intensity. This trend is illustrated in Fig. 82.35, where the average near-field intensity is given by

$$I_{avg} \equiv \frac{U_{shot}}{t_{eq} \cdot \pi \cdot r_{eq}^2}, \qquad (9)$$

where U_{shot} is the measured shot energy, the equivalent radius r_{eq} was defined in Eq. (4), and the equivalent pulse width t_{eq} was defined in Eq. (5). These values are tabulated in Table 82.IV for different pulse widths and energies. When the average near-field intensity is increased, both the small-spatial-scale and whole-beam B-integrals grow (since the small-

TC5339
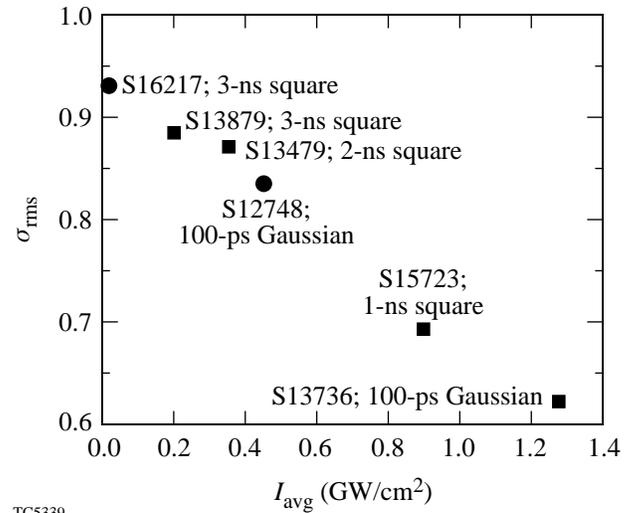
Figure 82.35
The nonuniformity as a function of average intensity for low- and high-energy versions of the pulse shapes. This figure illustrates the trend in the nonuniformity of UVETP images as a function of various pulse shapes and energies. The squares (■) represent the high-energy shots, and the circles (●) correspond to the low-energy counterparts. The points are labeled with the OMEGA shot numbers. Note the suppressed zero.

spatial-scale *B*-integral scales with the whole-beam *B*-integral), which in turn results in a lower measured value of σ_{rms}. For example, the peak whole-beam *B*-integral calculated for the 12.5-J, 100-ps Gaussian pulse increased from 4.64 rad to 9.99 rad (see Table 82.IV) when the energy of the 100-ps pulse was increased by a factor of 3, and the measured σ_{rms} decreased from 83.4% to 62.3%.

Power spectra of measured UVETP images are overplotted in Fig. 82.36 for three types of OMEGA shots without applied FM: a low-energy, 3-ns square pulse is overplotted with a high-energy, 100-ps Gaussian pulse in Fig. 82.36(a) and the same low-energy pulse is overplotted with a high-energy, 1-ns square pulse in Fig. 82.36(b). These spectra represent the three distinct types measured for no-FM pulses. The low-energy, 3-ns
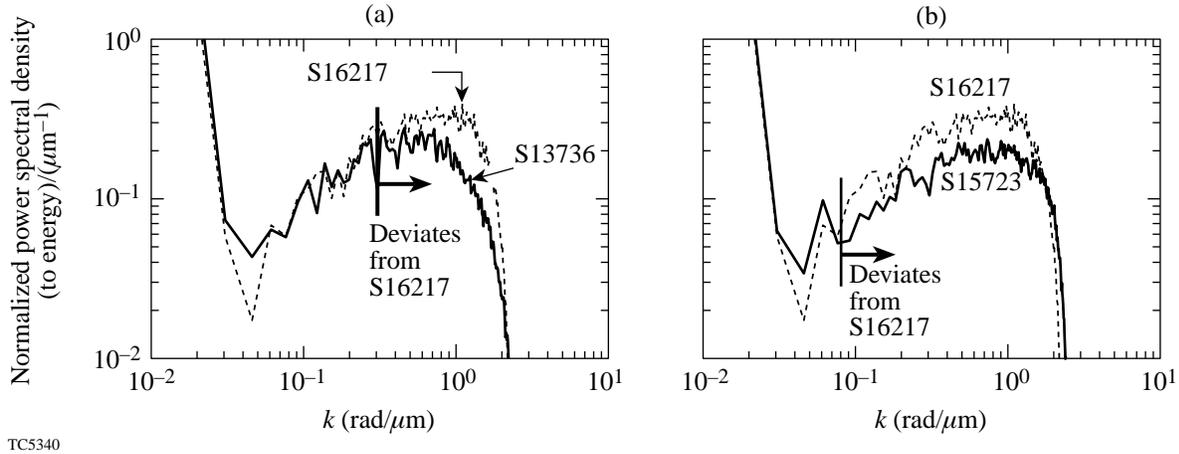
Figure 82.36

The 1-D power spectrum of UVETP images for (a) low-energy, 3-ns square (shot 16217; dashed line) and 100-ps Gaussian (shot 13736; solid black line) shots and (b) low-energy, 3-ns square (shot 16217; dashed line) and high-energy 1-ns square (shot 15723; solid black line). The low-energy shot was 5 J and represents the expected spectrum for shots without applied FM. The high-energy shots were 508 J and 40 J, respectively, and illustrate the smoothing effects of whole-beam and small-spatial-scale *B*-integrals in the regions indicated where the spectral power has been reduced relative to the low-energy shot.

Table 82.IV: Far-field analysis results from typical UVETP images and the *Waasikwa'* simulations that match the near-field conditions for a variety of pulse shapes and energies. A square-Hamming window shape was used. The UVETP image was cropped to span 720×720 pixels and covers 0.411×0.411 mm. The *Waasikwa'* simulation was cropped to match the area of the UVETP image so that it spans 424×424 pixels. Note that this yields identical speckle-frequency spacing of $dk_{ff} = 0.0153$ (rad/μm) for the measurement and simulation.

Shot Number	Nominal Pulse Width	Output-Pulse Shape	UV Beam Energy (J)	*RAINBOW* Calculated r_{eq} (cm)	*RAINBOW* Calculated t_{eq} (ns)	*RAINBOW* Peak Whole-Beam *B*-Integral (radians)	UVETP σ_{rms} (%)	*Waasikwa'* σ_{rms} (%) Whole-Beam *B*-Integral	*Waasikwa'* σ_{rms} (%) Whole-Beam and Small-Spatial-Scale *B*-Integrals
S12748	100 ps	Gaussian	12.5	7.76	0.126	4.64	83±0.5	96.3	94.1
S13736	100 ps	Gaussian	40	8.53	0.116	9.99	62±3	86.2	67.0
S15723	1 ns	square	508	12.6	0.964	20.0	69±5	95.2	69.9
S13479	2 ns	square	370	12.4	1.86	11.1	87±3	96.4	86.5
S16217	3 ns	square	6.6	7.09	2.98	0.970	93±1	98.0	98.9
S13879	3 ns	square	331	12.4	2.880	7.58	88±1	97.7	88.6

square shot without applied FM has a measured nonuniformity $\sigma_{rms} = 93\%$ near the 100% modulation expected for a DPP without *B*-integral effects. The high-energy shots exhibit nonuniformity values σ_{rms} from 62% to 88%. The 1-D power spectra of the 100-ps Gaussian high-energy shot deviate from the theoretical low-energy case over the spatial-frequency range $k_{ff} > 0.3(\text{rad}/\mu\text{m})$, as seen in Fig. 82.36(a), which corresponds to $\ell > 150$ and a full-angle near-field laser divergence of about 12 μrad. This pulse has insufficient time to smooth lower spatial frequencies. Conversely, the 1-D power spectra of the high-energy, 1-ns square shot deviates over a larger spatial-frequency range $k_{ff} > 0.08(\text{rad}/\mu\text{m})$ ($\ell > 40$), as seen in Fig. 82.36(b), even though this pulse has a lower average intensity and higher nonuniformity. For both cases, the deviation from the low-energy spectrum becomes significant, i.e., a ratio greater than about $\sqrt{2}$ for $k_{ff} > 0.7$ (rad/μm) ($\ell > 350$), which corresponds to a full-angle, near-field laser divergence of about 4 μrad. The other two high-energy square pulses, given in Table 82.IV, exhibit power spectra characteristics similar to the 1-ns case except that the power spectra show less deviation from the low-energy spectrum.

A comparison of the power spectra for the experimental measurements and the simulations demonstrates the smoothing effect of the small-spatial-scale and whole-beam *B*-integrals. The details of the *B*-integral modeling are given in the **Laser Beam Smoothing** section. The power spectra of the UVETP images are shown in Fig. 82.37 through Fig. 82.40 (as

solid gray lines) for the 100-ps, 1-ns, 2-ns, and 3-ns pulses with no FM, respectively. The figures include the resultant 1-D power spectra from corresponding *Waasikwa* simulations that include only whole-beam *B*-integral and both small-spatial-scale and whole-beam *B*-integral effects. Each power spectrum is normalized to the spectral energy of the 1-D power spectrum. The measured σ_{rms} is the lowest for the 100-ps pulse at 62.3% and increases with increasing pulse length up to 88.4% for the 3-ns pulse. The values of the nonuniformity σ_{rms} for all the UVETP images are summarized in Table 82.IV. The UVETP diagnostic was configured with a Gaussian-like DPP, which is fabricated to produce a far-field spot with an $N = 2.5$ super-Gaussian spatial-intensity envelope, for all of the shots except the 3-ns pulse. A higher-order DPP, which is fabricated to produce a far-field spot with an $N = 6.5$ super-Gaussian spatial-intensity envelope, was installed for the 3-ns pulse. The spatial-intensity envelope of the far field determines the low-wave-number power spectrum but does not significantly affect the large-wave-number power spectrum. The data windowing occludes the low-wave-number power spectra differences between the two DPP designs.

Simulations of the power spectra demonstrate that temporally varying local phase distortions in the beam caused by small-spatial-scale and whole-beam *B*-integral effects in the laser decrease the nonuniformity to levels that match the experimental results in pulses with no applied FM. The theoretical predictions of the models that include both of the
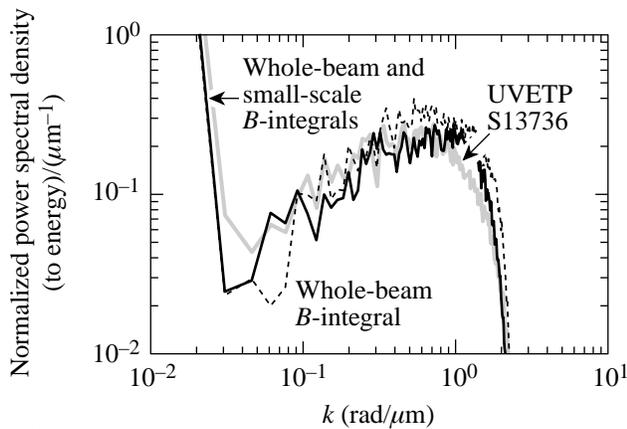
Figure 82.37
The 1-D power spectrum of a UVETP image of a 100-ps Gaussian pulse (shot 13736; solid gray line) and the corresponding *Waasikwa'* simulation including only whole-beam *B*-integral effects (dashed line) and both small-spatial-scale and whole-beam *B*-integral effects (solid black line).
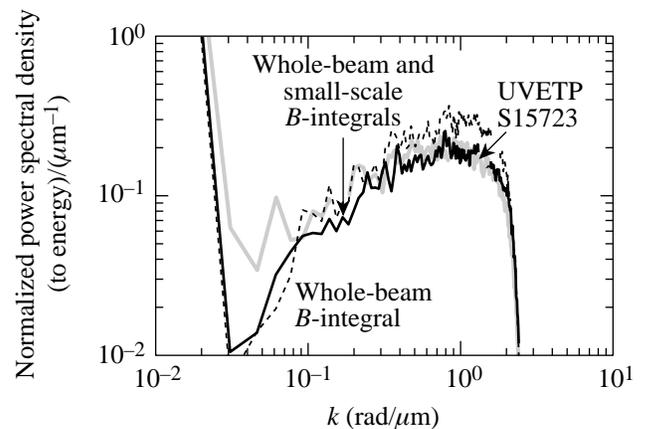
Figure 82.38
The 1-D power spectrum of a UVETP image of a 1-ns square pulse (shot 15723; solid gray line) and the corresponding *Waasikwa'* simulation including only whole-beam *B*-integral effects (dashed line) and both small-spatial-scale and whole-beam *B*-integral effects (solid black line).

B-integral effects are in excellent agreement with the measured power spectra for the 1-ns, 2-ns, and 3-ns square pulses over the range of $k_{ff} > 0.1$ rad/μm. There is a slight discrepancy for the combined B-integral model due to excess smoothing over the range of $0.1 < k_{ff} < 0.3$ rad/μm. The 100-ps Gaussian simulations are limited by the near-field measurements as described in the next section. The impact of the small-spatial-scale B-integral effects (solid black line) on the power spectrum is evident in Figs. 82.37–82.40, where the simulations (dashed line) that model the whole-beam B-integral effects but neglect the small-spatial-scale B-integral effects are shown. The effects of the whole-beam B-integral reduce the σ_{rms} to a level of 86.2% and 95.2% for the 100-ps and 1-ns high-energy pulses, respectively, which does not match the experimental results with $\sigma_{rms} = 62\%$ for the 100-ps pulse and $\sigma_{rms} = 69.3\%$ for the 1-ns pulse. The combined effects of the whole-beam and small-spatial-scale B-integrals, however, reduce the σ_{rms} to a level of 67.0% and 69.9% for the 100-ps and 1-ns high-energy pulses, respectively, which is comparable to the experimental values. The values of the nonuniformity σ_{rms} for all the *Waasikwa'* simulations are summarized in Table 82.IV.

Laser Beam Smoothing

Smoothing in the far field occurs when the state of the transverse phase front of the near field, given by $\phi(x,y,t)$, changes as a function of time such that the spatial coherence is altered. For a particular instant in time, a state $\phi(x,y,t)$ will produce a unique speckle pattern in accordance with the statistics of the DPP. If the state of $\phi(x,y,t)$ changes in time over an interval $\tau \equiv t_2 - t_1$ (where τ is of the order of the coherence time for the pulse) such that a change in state $\Delta\phi(x,y,\tau)$ $\equiv \phi(x,y,t_2) - \phi(x,y,t_1)$ is nonconstant over the near field, the instantaneous far-field speckle pattern will change, resulting in time-integrated smoothing. Alternately, if the quantity $\Delta\phi(x,y,\tau)$ is constant over the near field, during the time interval τ, then no change in the far-field speckle pattern occurs regardless of how rapidly the state $\phi(x,y,t)$ varies in space or time. For example, a nondispersed phase-modulated pulse can be represented by $\phi(x,y,t) = \phi_1(x,y) + \phi_2(t)$.

Time-integrated smoothing in the far field can be understood as a movement of the speckle structure or as a distinct change of the speckle structure as a function of time. If the change in state $\Delta\phi(x,y,\tau)$ has a linear form, i.e.,

$$\Delta\phi(x,y,\tau) \equiv x(\partial\phi/\partial x) + y(\partial\phi/\partial y),$$

then the speckle pattern will appear to laterally shift in the far field by the amounts given by $\Delta x_{ff} = f_\Omega(\partial\phi/\partial x)$ and $\Delta y_{ff} = f_\Omega(\partial\phi/\partial y)$. In the more general case, the phase-state $\phi(x,y,t)$ can be Fourier decomposed into a set of modes as

$$\phi(x,y,t) \equiv \frac{1}{4\pi^2} \iint_{\substack{\forall \text{spatial} \\ \text{frequencies}}} \tilde{\phi}(k_x,k_y,t)e^{+i(k_x x + k_y y)}dk_x dk_y, \quad (10)$$
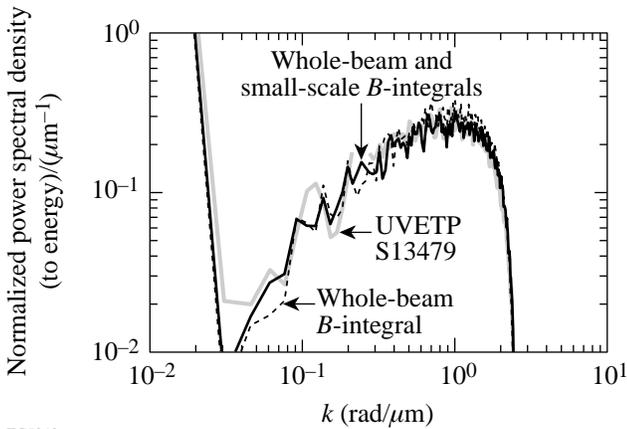
Figure 82.39
The 1-D power spectrum of a UVETP image of a 2-ns square pulse (shot 13479; solid gray line) and the corresponding *Waasikwa'* simulation including only whole-beam B-integral effects (dashed line) and both small-spatial-scale and whole-beam B-integral effects (solid black line).
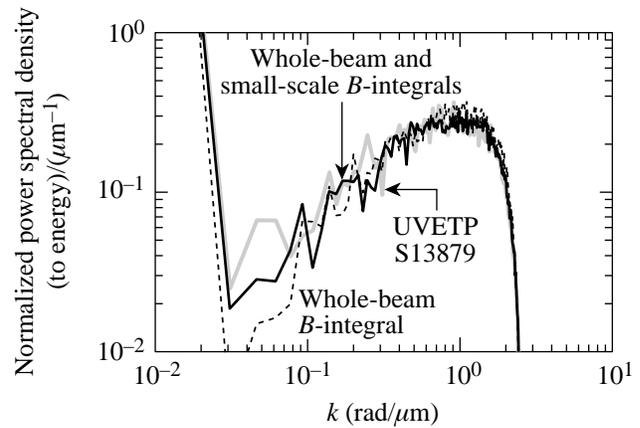
Figure 82.40
The 1-D power spectrum of a UVETP image of a 3-ns square pulse (shot 13879; solid gray line) and the corresponding *Waasikwa'* simulation including only whole-beam B-integral effects (dashed line) and both small-spatial-scale and whole-beam B-integral effects (solid black line).

where $\tilde{\phi}(k_x, k_y, t)$ represents the complex spectral amplitudes of the Fourier kernel $e^{+i(k_x x + k_y y)}$. At each instant in time $\phi(x, y, t) \in \mathbb{R}$, which implies that the integral in Eq. (10) may be reduced to two times the real part of the integral over the upper half-plane that excludes the negative axis owing to the symmetry properties of the Fourier transform of real functions [i.e., the transform is Hermitian $\tilde{\phi}(k_x, k_y, t) = \phi^*(-k_x, -k_y, t)$ (Ref. 18, p. 14)].

The smoothing effectiveness of an evolving phase state $\phi(x, y, t)$ can be understood by examining the contribution of the term $e^{i\phi(x, y, t)}$ to the far-field distribution. The instantaneous far-field speckle pattern is calculated by Eq. (2). The convolution theorem dictates that the result can be written as

$$I_{\text{ff}}(x_{\text{ff}}, y_{\text{ff}}, t) = \left| E_{\text{DPP}}(x_{\text{ff}}, y_{\text{ff}}, t) * E_\phi(x_{\text{ff}}, y_{\text{ff}}, t) \right|^2, \quad (11)$$

where the quantity $E_{\text{DPP}}(x_{\text{ff}}, y_{\text{ff}}, t)$ represents the complex field of the speckle pattern caused by the combined effect of the current beam cross section and the DPP; the quantity $E_\phi(x_{\text{ff}}, y_{\text{ff}}, t)$ represents the instantaneous complex far-field pattern caused by the phase state $\phi(x, y, t)$; and the symbol * denotes the convolution operation. The extent of the far-field pattern $E_\phi(x_{\text{ff}}, y_{\text{ff}}, t)$ determines the wavelengths that can be smoothed: the greater the area covered, the longer the wavelengths that the phase state $\phi(x, y, t)$ can smooth. The far-field pattern $E_\phi(x_{\text{ff}}, y_{\text{ff}}, t)$ must change over time to affect smoothing. Further, the pulse must be long enough to cover many coherence times: the longer the wavelength, the more smoothing time required.

$$\phi(x, y, t)$$
$$= 2\left| \tilde{\phi}(k_x, k_y, t) \right| \sin\left(\measuredangle\{\tilde{\phi}(k_x, k_y, t)\} + k_x x + k_y y \right), \quad (12)$$

where the term $\left| \tilde{\phi}(k_x, k_y, t) \right|$ represents the magnitude of the Fourier component and the term $\measuredangle\{\tilde{\phi}(k_x, k_y, t)\}$ represents the phase [where the operator $\measuredangle\{e^{i\theta}\} = \theta$]. The term $\left| \tilde{\phi}(k_x, k_y, t) \right|$ determines the amount of laser divergence, given approximately by

$$\Delta\theta \cong 2\left[\left| \tilde{\phi}(k_x, k_y, t) \right| + 1 \right] \sqrt{k_x^2 + k_y^2}.$$

If the quantity $\left| \tilde{\phi}(k_x, k_y, t) \right| = \delta_m$, where δ_m is constant and $\measuredangle\{\tilde{\phi}(k_x, k_y, t)\} = \omega_m t$, then Eq. (12) is functionally identical to 1-D SSD.[20] In this scenario, the spectral components of $E_\phi(x_{\text{ff}}, y_{\text{ff}}, t)$ in the far field have fixed amplitudes and a fixed

spacing (given by the well-known Bessel function expansion; see Ref. 20) but a varying relative phase. If the magnitude of the phase varies in time as $\left| \tilde{\phi}(k_x, k_y, t) \right| = \delta_m(t)$ and if the phase term $\measuredangle\{\tilde{\phi}(k_x, k_y, t)\}$ is constant, the spectral components of $E_\phi(x_{\text{ff}}, y_{\text{ff}}, t)$ in the far field have a fixed spacing analogous to the SSD-like case but with a varying amplitude and a fixed relative phase. As the magnitude $\delta_m(t)$ increases, the number of the spectral components increases and spreads out into the far field (this situation is directly analogous to what happens when the whole-beam B-integral modifies the phase magnitude where the Fourier component's wavelength is twice the beam diameter). A general case is constructed when both the magnitude and phase terms in Eq. (12) are allowed to vary with time. A stochastic model may also be employed where the magnitude and relative phase terms change in time of the order of the coherence time and obey a probability density function.

If more than one spectral mode is considered, a variety of complex smoothing mechanisms can be constructed. However, an arbitrary phase state that alters the spatial coherence over time and, in addition, is consistent with the observations cannot be selected. When considering a small number of Fourier components, the member with the greatest laser divergence can be assumed to dominate the remaining members since its laser divergence will be the strongest (see Ref. 21, p. 241 regarding transmission bandwidth). Otherwise, the total divergence of each member must be considered in terms of their combined effect as they convolve together in the far field and produce a greater spread and smooth longer wavelengths. To this end, the dominant mode will contribute a full-angle divergence of $\Delta\theta \cong 2[\delta_m(t) + 1]\sqrt{k_x^2 + k_y^2}$ and a temporal bandwidth $\Delta\omega \cong [\delta_m(t) + 1]\omega_m$, and the other modes will contribute significantly only if their respective spatial or temporal bandwidths are comparable to the dominant mode. The maximum far-field wavelength that can be smoothed is given by $S_{\text{max}} = f_\Omega \Delta\theta$. The situation is analogous to the small-spatial-scale B-integral when the Fourier components have a fixed phase relationship (i.e., they do not move across the near field) and the modulation depth (of each spectral component) changes as the pulse evolves.

1. Whole-Beam B-Integral Modeling

The electric field and phase calculated by *RAINBOW* for a pulsed beam are in cylindrical coordinates, viz. (r,t). Conversely, *Waasikwa'* models both transverse dimensions and time in rectangular cartesian coordinates, viz. (x,y,t). Accordingly, a two-dimensional spline fit is performed at each time step to resample *RAINBOW* data into cartesian coordinates. The complex-valued electric field with no applied FM or DPP

that describes the UV near field is expressed in terms of the converted *RAINBOW* data as

$$E(x,y,t) \equiv E_{0_{\text{rb}}}(x,y,t) e^{i\phi_{B_{\text{rb}}}(x,y,t)}. \tag{13}$$

The phase term $\phi_{B_{\text{rb}}}(x,y,t)$ calculated by *RAINBOW* represents the whole-beam *B*-integral that is an intensity-dependent phase accumulated during propagation within a nonlinear medium.

The phase state calculated by *RAINBOW* is roughly separable, i.e., $\phi_{B_{\text{rb}}}(x,y,t) \cong \delta_{B_{\text{rb}}}(t)\phi_{B_{\text{rb}}}(x,y)$. The quantity $\phi_{B_{\text{rb}}}(x,y)$ represents the initial beam shape that is injected into the laser chain, and the term $\delta_{B_{\text{rb}}}(t)$ represents the initial pulse shape. This occurs because of self-phase modulation in the laser chain that is more severe in the first amplifiers where the local intensity is higher and prior to significant gain saturation that causes the intensity beam profile to change over time. In other words, even though the intensity envelope is altered after the whole laser chain, the phase modulation retains a shape very similar to that of the injected beam. (The form of the phase state is analogous to that discussed in the previous section, where the spatial portion of a mode is fixed and the modulation depth changes over time.) Therefore, the laser divergence causes the far field to expand as a function of time. This effect for a 100-ps Gaussian pulse is illustrated in

TC5345
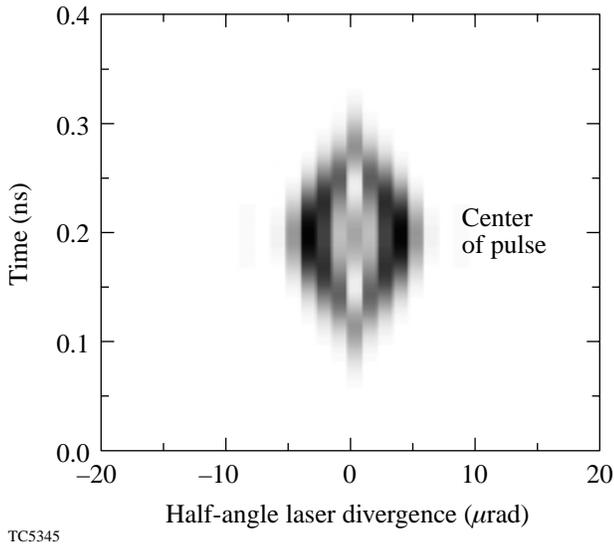
Figure 82.41
The calculated laser divergence due to the whole-beam *B*-integral as a function of time for a 40-J, 100-ps Gaussian pulse.

Fig. 82.41, where the laser divergence is plotted against time. Based on the calculated laser divergence one would expect that the whole-beam *B*-integral would smooth down to the far-field spatial frequency,

$$k_{\text{ff}} = \frac{2\pi}{f_\Omega \Delta\theta} \approx 0.35 \frac{\text{rad}}{\mu\text{m}},$$

from the calculated full-angle divergence of $\Delta\theta \approx 10 \, \mu\text{rad}$ (see Fig. 82.41). As shown in the **Experimental Results** section the nonuniformity calculated with this model, however, falls short of the measured smoothing. Additionally, the power spectrum (dashed line in Fig. 82.37) is almost identical to the low-energy pulse (dashed line in Fig. 82.36). The primary reason is that although there is sufficient laser divergence, the temporal bandwidth for this method is insufficient to produce a short coherence time because the peak *B*-integral is limited. This model also fails to predict the measured nonuniformity and power spectra for the square pulses for the same reasons.

2. Modeling of Small-Spatial-Scale and Whole-Beam
   B-Integrals
   Near-field images of high-energy shots were obtained in the UV section of the OMEGA system (measured after the final amplifiers and after the FCC's). Two pulse lengths—a 100-ps Gaussian [Fig. 82.42(a)] and a 1-ns square [Fig. 82.42(b)]—were captured to compare the fluence of the early times to that at later times. The 100-ps Gaussian near field was representative of a center-peaked beam; the 1-ns square pulse was representative of an edge-peaked beam. These images revealed evidence of small-spatial-scale intensity ripple across the beam, which was more severe for the shorter pulse than the longer pulse because of gain-saturation effects. This evidence has led to speculation that the small-spatial-scale *B*-integral caused the observed smoothing; the depth of the fluence ripple corresponds to the laser divergence required to affect the smoothing in the range $k_{\text{ff}} > 0.1$ (rad/μm), and the growth of the ripple provides the required temporal bandwidth.

The small-spatial-scale and whole-beam *B*-integral phases both result from self-phase modulation, which is proportional to the local accumulated intensity of the beam as it propagates through a nonlinear medium. The combined phase effects of the small-spatial-scale and whole-beam *B*-integrals can be inferred from the fluence measured by the near-field images. The time evolution of the small-spatial-scale *B*-integral can be approximated to follow the spatiotemporal evolution of the whole-beam *B*-integral that is calculated by *RAINBOW*. This is

only valid, however, over a small energy range neighboring the measured near field because the ripple across the beam becomes less pronounced as saturation becomes important. For long, high-energy (fluence) pulses, the beam experiences significant gain saturation in the system amplifiers. The beam profile is smoothed at later times in the pulse because the amount of gain saturation at any spatial location in the beam is proportional to the beam's fluence at that location; initially "hotter" regions of the beam experience reduced gain. This effect is modeled by temporally blending different measured near fields.
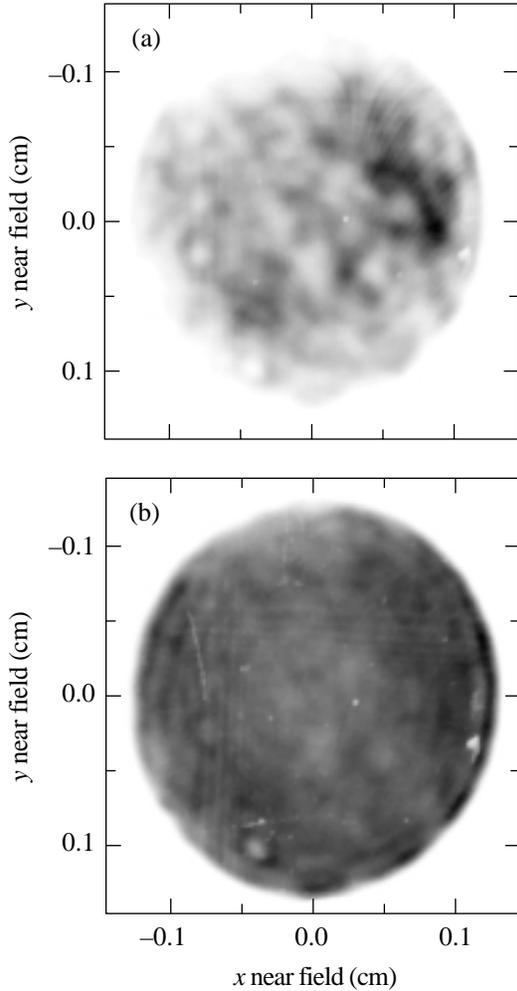
TC5346

Figure 82.42
Two near-field fluence measurements, taken after the FCC's, represent the early- and late-time evolution of a long pulse. (a) The first image (shot 14233) is a 100-ps Gaussian pulse representative of the early-time evolution. (b) The second image (shot 14234) is a 1-ns square pulse representative of the late-time evolution.

A model of combined *B*-integral effects is constructed by perturbing both the intensity and phase calculated by *RAINBOW* simulations. The electric field of the near field is expressed as [compare Eq. (3)]

$$E_{\text{sim}}(x,y,t) \equiv E_{0_{\text{sim}}}(x,y,t)e^{i\phi_{B_{\text{sim}}}(x,y,t)}, \qquad (14)$$

where the perturbed magnitude of the electric field is defined by

$$E_{0_{\text{sim}}}(x,y,t) \equiv E_{0_{\text{rb}}}(x,y,t)\sqrt{\Gamma(x,y)}, \qquad (15)$$

and the perturbed phase contribution due to both small-spatial-scale and whole-beam *B*-integral effects is given by

$$\phi_{B_{\text{sim}}}(x,y,t) \equiv \phi_{B_{\text{rb}}}(x,y,t)\Gamma(x,y). \qquad (16)$$

The unperturbed magnitude and phase of the electric field calculated by *RAINBOW* simulations are given in Eqs. (15) and (16) by $E_{0_{\text{rb}}}(x,y,t)$ and $\phi_{B_{\text{rb}}}(x,y,t)$, respectively. The perturbation function $\Gamma(x,y)$ represents the scaled ratio of a UV near-field fluence measurement to the fluence calculated from a *RAINBOW* simulation, namely

$$\Gamma(x,y) \equiv \alpha \frac{F_{\text{UVnf}}(x,y)}{F_{\text{rb}}(x,y)}, \qquad (17)$$

where the subscript UVnf indicates the UV near-field measurement, the subscript rb indicates the *RAINBOW* simulation, and α is the proportionality constant and is defined by

$$\alpha \equiv \frac{W_{\text{rb}}}{W_{\text{UVnf}}}, \qquad (18)$$

where W_{rb} is the *RAINBOW* simulation energy and W_{UVnf} is the UV near-field energy.

The two UV near-field measurements are blended temporally to construct a model for longer, higher-energy pulses. The UV near-field measurements are used to divide the longer pulse into segments based on the energy within each measured UV near field. The techniques described previously are employed to evaluate the perturbation function within each temporal segment. The blending function is defined as a dimensionless and smooth step function:

$$b(\tau_{\mathrm{on}}, \tau_{\mathrm{off}}, r, t)$$

$$\equiv \frac{1}{2}\left\{\tanh\left[r(t - \tau_{\mathrm{on}})\right] - \tanh\left[r(t - \tau_{\mathrm{off}})\right]\right\}, \qquad (19)$$

where τ_{on} and τ_{off} are the turn-on and turn-off times and r is the rate at which the blending function mixes the UV near fields. The dividing time of the segments is defined when the *RAINBOW* simulation has equivalent energy to a UV near-field measurement:

$$W_{\mathrm{UVnf}_n} \equiv \int_0^{\tau_n} \iint\limits_{\substack{\mathrm{near} \\ \mathrm{field}}} I_{\mathrm{rb}}(x, y, t)\, dx\, dy\, dt, \qquad (20)$$

where the subscript n refers to a particular near field, e.g., $n = 1$ for the first UV near field. The times τ_n define the turn-on and turn-off times for the blending function; one blending function turns off as the next one turns on, e.g., the first blending function is $b(-\infty, \tau_1, r, t)$ and the second is $b(\tau_1, \tau_2, r, t)$. The final blending function mixes into unperturbed *RAINBOW* data with $b(\tau_2, \infty, r, t)$. Energy conservation requires that

$$\sum_{n=1}^{3} b\left(\tau_{\mathrm{on}_n}, \tau_{\mathrm{off}_n}, r, t\right) = 1;\ \forall t. \qquad (21)$$

The time difference between τ_1 and τ_2 will change according to the modeled pulse. As the differential $\Delta\tau = \tau_2 - \tau_1$ decreases, the mixing rate r increases, which effectively describes how the small-spatial-scale perturbations change more rapidly. The decreased $\Delta\tau$ occurs physically because the saturation fluence is reached earlier for the higher-intensity pulses. The mixing rate is adjusted to eliminate any step that may be introduced in the nonuniformity as a function of time. The switching times and mixing rates for the different modeled pulses are given in Table 82.V.

The calculated laser divergence for this model as a function of time is illustrated in Fig. 82.43 for a 1-ns square pulse at full-system energy. This modeling scheme works well for the longer square pulses but does not adequately describe the smoothing observed for the shorter, 100-ps pulses. This is attributed to the fact that the early time evolution of the small-scale B-integral is not captured on either measured near field, and consequently, only a single UV near field is used.
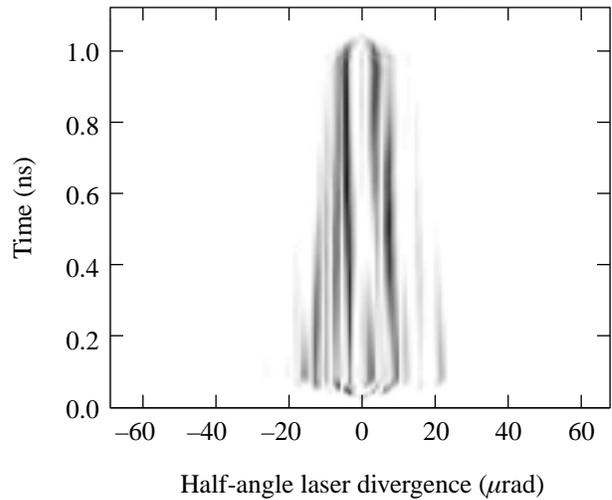
TC5347

Figure 82.43
The calculated laser divergence due to the whole-beam and small-spatial-scale B-integrals as a function of time for a 1-ns square pulse at full system energy.

Table 82.V: Summary of the model parameters for 1-ns, 2-ns, and 3-ns square pulses. The parameters τ_1 and τ_2 define when the *RAINBOW* simulation has energy equivalent to the first and second UV near field, respectively. The energy of the first UV near field is 100 J; the energy of the second UV near field is 290 J.

Shot Number	Nominal Pulse Width (ns)	Measured Energy (J)	τ_1 for 100 J (ns)	τ_2 for 290 J (ns)	r (1/ns)
S15723	1	508	0.225	0.555	1.92
S13479	2	370	0.645	1.57	1.12
S13879	3	331	1.18	2.99	0.775

Conclusion

The observed smoothing on high-energy OMEGA shots without applied FM has been successfully modeled using a combination of small-spatial-scale and whole-beam *B*-integral effects. The smoothing affects mainly the spatial wave numbers $k_{ff} > 0.1(\text{rad}/\mu\text{m})$ and can reduce the nonuniformity to levels of 62%. The nonuniformity decreases approximately linearly with increasing average intensity of the pulsed beam. The amount of smoothing due to small-spatial-scale *B*-integral effects is insufficient for direct-drive ICF. Reference 13 shows that smoothing by spectral dispersion overwhelms this effect in the mid-range spatial frequencies where these modes are considered the most dangerous spatial frequencies for ICF implosions.[7] Hence, it is not expected that the *B*-integral effects mitigate hydrodynamic instabilities due to their minor influence.

REFERENCES

1. C. P. Verdon, Bull. Am. Phys. Soc. **38**, 2010 (1993).

2. S. E. Bodner, D. G. Colombant, J. H. Gardner, R. H. Lehmberg, S. P. Obenschain, L. Phillips, A. J. Schmitt, J. D. Sethian, R. L. McCrory, W. Seka, C. P. Verdon, J. P. Knauer, B. B. Afeyan, and H. T. Powell, Phys. Plasmas **5**, 1901 (1998).

3. D. K. Bradley, J. A. Delettrez, and C. P. Verdon, Phys. Rev. Lett. **68**, 2774 (1992); J. Delettrez, D. K. Bradley, and C. P. Verdon, Phys. Plasmas **1**, 2342 (1994); J. D. Kilkenny, S. G. Glendinning, S. W. Haan, B. A. Hammel, J. D. Lindl, D. Munro, B. A. Remington, S. V. Weber, J. P. Knauer, and C. P. Verdon, Phys. Plasmas **1**, 1379 (1994); R. Epstein, J. Appl. Phys. **82**, 2123 (1997); V. A. Smalyuk, T. R. Boehly, D. K. Bradley, V. N. Goncharov, J. A. Delettrez, J. P. Knauer, D. D. Meyerhofer, D. Oron, and D. Shvarts, Phys. Rev. Lett. **81**, 5342 (1998).

4. F. J. Marshall and G. R. Bennett, Rev. Sci. Instrum. **70**, 617 (1999); F. J. Marshall, J. A. Delettrez, V. Yu. Glebov, R. P. J. Town, B. Yaakobi, R. L. Kremens, and M. Cable, Phys. Plasmas **7**, 1006 (2000).

5. T. R. Boehly, D. L. Brown, R. S. Craxton, R. L. Keck, J. P. Knauer, J. H. Kelly, T. J. Kessler, S. A. Kumpan, S. J. Loucks, S. A. Letzring, F. J. Marshall, R. L. McCrory, S. F. B. Morse, W. Seka, J. M. Soures, and C. P. Verdon, Opt. Commun. **133**, 495 (1997).

6. S. Skupsky, R. W. Short, T. Kessler, R. S. Craxton, S. Letzring, and J. M. Soures, J. Appl. Phys. **66**, 3456 (1989).

7. Laboratory for Laser Energetics LLE Review **69**, 1, NTIS document No. DOE/SF/19460-152 (1996) (Copies may be obtained from the National Technical Information Service, Springfield, VA 22161); S. Skupsky and R. S. Craxton, Phys. Plasmas **6**, 2157 (1999).

8. J. E. Rothenberg, J. Opt. Soc. Am. B **14**, 1664 (1997).

9. T. J. Kessler, Y. Lin, J. J. Armstrong, and B. Velazquez, in *Laser Coherence Control: Technology and Applications*, edited by H. T. Powell and T. J. Kessler (SPIE, Bellingham, WA, 1993), Vol. 1870, pp. 95–104.

10. Y. Lin, T. J. Kessler, and G. N. Lawrence, Opt. Lett. **21**, 1703 (1996).

11. Y. Kato, unpublished notes (1984); K. Tsubakimoto *et al.*, Opt. Commun. **91**, 9 (1992); K. Tsubakimoto *et al.*, Opt. Commun. **103**, 185 (1993).

12. Laboratory for Laser Energetics LLE Review **45**, 1, NTIS document No. DOE/DP40200-149 (1990) (Copies may be obtained from the National Technical Information Service, Springfield, VA 22161); T. E. Gunderman, J.-C. Lee, T. J. Kessler, S. D. Jacobs, D. J. Smith, and S. Skupsky, in *Conference on Lasers and Electro-Optics*, Vol. 7, 1990 OSA Technical Digest Series (Optical Society of America, Washington, DC, 1990), p. 354.

13. S. P. Regan, J. A. Marozas, J. H. Kelly, T. R. Boehly, W. R. Donaldson, P. A. Jaanimagi, R. L. Keck, T. J. Kessler, D. D. Meyerhofer, W. Seka, S. Skupsky, and V. A. Smalyuk, "Experimental Investigation of Smoothing by Spectral Dispersion," to be published in the Journal of the Optical Society of America B.

14. A. E. Siegman, *Lasers* (University Science Books, Mill Valley, CA, 1986).

15. D. C. Brown, in *High-Peak-Power Nd:Glass Laser Systems*, edited by D. L. MacAdam, Springer Series in Optical Sciences (Springer-Verlag, Berlin, 1981), Vol. 25.

16. D. Cortesi, *Topics in IRIX® Programming*, Document Number 007-2478-007, Silicon Graphics, Inc., Mountain View, CA, 1999.

17. J. W. Goodman, *Introduction to Fourier Optics* (McGraw-Hill, New York, 1968).

18. R. N. Bracewell, *The Fourier Transform and Its Applications*, 2nd ed., rev., McGraw-Hill Series in Electrical Engineering. Circuits and Systems (McGraw-Hill, New York, 1986).

19. J. G. Proakis and D. G. Manolakis, *Introduction to Digital Signal Processing* (Macmillan, New York, 1988).

20. Laboratory for Laser Energetics LLE Review **78**, 62, NTIS document No. DOE/SF/19460-295 (1999). Copies may be obtained from the National Technical Information Service, Springfield, VA 22161.

21. A. B. Carlson, *Communication Systems: An Introduction to Signals and Noise in Electrical Communication*, McGraw-Hill Electrical and Electronic Engineering Series (McGraw-Hill, New York, 1968), p. 154.